PHYSICAL REVIEW B **93**, 195440 (2016)

Theoretical aspects of the Edelstein effect for anisotropic two-dimensional electron gas and topological insulators

Annika Johansson,[1,2,*] Jürgen Henk,[2] and Ingrid Mertig[1,2]
[1]*Max Planck Institute of Microstructure Physics, Weinberg 2, 06120 Halle, Germany*
[2]*Institute of Physics, Martin Luther University Halle-Wittenberg, 06099 Halle, Germany*
(Received 4 March 2016; revised manuscript received 28 April 2016; published 26 May 2016)

A charge current driven through a two-dimensional electron gas (2DEG) with Rashba spin-orbit coupling generates a spatially homogeneous spin polarization perpendicular to the applied electric field. This phenomenon is the Aronov–Lyanda-Geller–Edelstein (ALGE) effect. For selected model systems, we consider the ALGE effect within the semiclassical Boltzmann transport theory. Its energy dependence is investigated, in particular the regime below the Dirac point of the 2DEG. In addition to an isotropic 2DEG, we analyze systems with anisotropic Fermi contours. We predict that the current-induced spin polarization vanishes if the Fermi contour passes through a Lifshitz transition. Further, we corroborate that topological insulators (TI) provide a very efficient charge-to-spin conversion.

DOI: 10.1103/PhysRevB.93.195440

I. INTRODUCTION

One promising effect providing charge-to-spin conversion in nonmagnetic materials is the Aronov–Lyanda-Geller–Edelstein (ALGE) effect, considered first in 1989 by Aronov and Lyanda-Geller [1] as well as Edelstein [2]. Often, it is called the Edelstein effect or inverse spin-galvanic effect [3]. In systems with broken inversion symmetry, such as surfaces or interfaces, spin-orbit coupling (SOC) lifts the spin degeneracy [4–6]. An in-plane electric current penetrating the system gives rise to a homogeneous in-plane spin polarization perpendicular to the applied electric field. Thus, a nonzero spin polarization is generated in nonmagnetic systems purely electrically.

Because of these promising properties, the ALGE effect has been the subject of numerous theoretical considerations [1–3,7–10]. Experimental evidence for the ALGE effect and its inverse has been given by several experimental methods [11–17].

In this paper we consider the ALGE effect in Rashba systems [4–6] within a two-dimensional free-electron model using the semiclassical Boltzmann transport theory [18]. This approach has been used for the description of the ALGE effect in systems with Rashba, Dresselhaus, and Luttinger SOC in a number of previous works [3,19–22]. However, the isotropic two-dimensional electron gas (2DEG) model addressed in Refs. [1–3,3,7–10,19–22] provides merely a rough approximation to real systems with reduced symmetry, such as (110) surfaces ($C_{2\mathrm{v}}$ symmetry) or (111) surfaces with a strong in-plane potential gradient ($C_{3\mathrm{v}}$ symmetry). In addition to the usually considered isotropic 2DEG, we discuss the ALGE effect in anisotropic systems with $C_{2\mathrm{v}}$ and $C_{3\mathrm{v}}$ symmetry within the entire energy range. Thus, this work is an extension of the intensely studied ALGE effect in isotropic Rashba systems since it addresses also systems with reduced symmetry. With respect to practical applications our purpose is to maximize the charge-to-spin conversion efficiency. Therefore, we investigate in which direction an external electric field should be applied in systems with $C_{2\mathrm{v}}$ symmetry to gain a large ALGE effect. This theoretical consideration is useful for experiments on the ALGE effect. Ast *et al.* [23] and Premper *et al.* [24] showed that an enormous Rashba splitting occurs in ordered surface alloys due to an additional in-plane potential gradient, which should be accompanied by a sizable ALGE effect. However, in those systems the in-plane symmetry is broken. We study the influence of this symmetry breaking on the ALGE effect.

Furthermore, the ALGE effect in the surface states of topological insulators (TIs) is examined because TIs are a promising material class for an effective charge-to-spin conversion [25]. We consider the surface states of TIs within a model similar to the Rashba Hamiltonian. Since a Rashba 2DEG and the surface states of TIs differ qualitatively, we discuss similarities and differences in the result for the current-induced spin density. We discuss also the ALGE effect for TIs with $C_{3\mathrm{v}}$ symmetry (e.g., Bi_2Se_3 and Bi_2Te_3) [26].

This paper is organized as follows. In Sec. II A a general model for the consideration of the ALGE effect in isotropic Rashba systems is introduced. Subsequently, this model is extended to systems with reduced symmetry (Sec. II B). In Sec. II C the ALGE effect in topological insulators is considered. The theoretical results are applied to selected real systems.

II. MODEL AND RESULTS

A. Isotropic systems

A two-dimensional free electron gas within the xy plane with Rashba spin-orbit coupling [5] is described by the Hamiltonian

$$\hat{H} = \frac{\hbar^2 \vec{k}^2}{2m} + \alpha_{\mathrm{R}} (\vec{e}_z \times \vec{k}) \cdot \vec{\sigma} \, , \tag{1}$$

where $\vec{k} = (k_x, k_y)$ is the in-plane momentum, m is the effective electron mass, $\vec{e}_z$ is the unit vector perpendicular to the 2DEG, and $\vec{\sigma}$ is the Pauli spin vector. The Rashba parameter α_{R} is a measure of the strength of the SOC. The energy eigenvalues

---

[*] ajohanss@mpi-halle.mpg.de

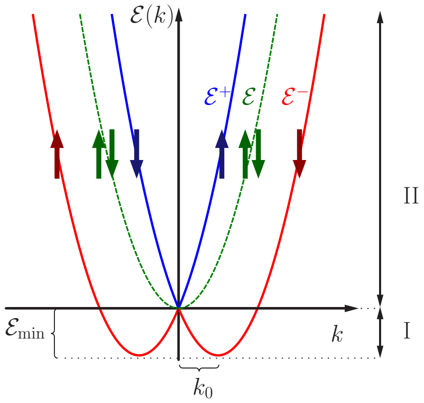

FIG. 1. Energy spectrum of a 2DEG with Rashba SOC (solid lines) for one direction in $\vec{k}$ space. Blue and red represent the $+$ and $-$ branches in Eq. (2), respectively. For comparison, the free-electron parabola without SOC is shown (dashed line). The arrows indicate the spin expectation values with respect to a quantization axis perpendicular to $\vec{k}$.

of the Hamiltonian (1) are

$$\mathcal{E}^{\pm}(\vec{k}) = \frac{\hbar^2 k^2}{2m} \pm \alpha_{\mathrm{R}} k \ , \qquad (2)$$

where $k = |\vec{k}|$. Due to the SOC, the energy parabola of free electrons is split into two parabolas which are shifted by $\mathcal{E}_{\text{min}} = -\alpha_{\mathrm{R}}^2 m / 2\hbar^2$, $k_0 = \pm \alpha_{\mathrm{R}} m / \hbar^2$, as shown in Fig. 1. The spin degeneracy is lifted except for the Dirac point ($k = 0, \mathcal{E} = 0$).

Corresponding to the $\pm$ sign of the k linear term in Eq. (2), two energy branches, $+$ and $-$, are defined. The $+$ branch exists only for $\mathcal{E} > 0$. We distinguish two energy regions: region I reaches from the band edge to the Dirac point; region II is above the Dirac point, as shown in Fig. 1. The lines of constant energy consist of two concentric circles in $\vec{k}$ space.

The eigenfunctions of the Hamiltonian (1) are spinors,

$$|\vec{k},\pm\rangle = \begin{pmatrix} \Psi_{\uparrow}^{\pm}(\vec{k}) \\ \Psi_{\downarrow}^{\pm}(\vec{k}) \end{pmatrix},$$

which are normalized and obey

$$\Psi_{\downarrow}^{\pm}(\vec{k}) = \pm i e^{i\varphi_{\vec{k}}} \Psi_{\uparrow}^{\pm}(\vec{k}), \qquad (3)$$

where $\varphi_{\vec{k}}$ is the azimuth of $\vec{k}$, $\cos\varphi_{\vec{k}} = k_x / x$. The spin expectation value $\langle\vec{\sigma}\rangle_{\vec{k}}^{\pm}$ of $|\vec{k},\pm\rangle$ is given by

$$\langle\vec{\sigma}\rangle_{\vec{k}}^{\pm} = \langle\vec{k},\pm|\hat{\vec{\sigma}}|\vec{k},\pm\rangle = \pm\frac{1}{k^{\pm}}(\vec{e}_z \times \vec{k}^{\pm}). \qquad (4)$$

Due to the inversion asymmetry, spin and orbital momentum are coupled. The $\vec{k}$-dependent spin expectation values at the Fermi energy are shown in Fig. 2(a). They are within the plane of the 2DEG, perpendicular to $\vec{k}$. The spin textures of the branches are clockwise ($-$ branch) and anticlockwise ($+$ branch).

For the consideration of the ALGE effect the expectation value of the total spin $\langle\vec{\sigma}\rangle$ is calculated by summation of the spin expectation values of all occupied states. For reasons of time-inversion symmetry, the total spin polarization vanishes in equilibrium.

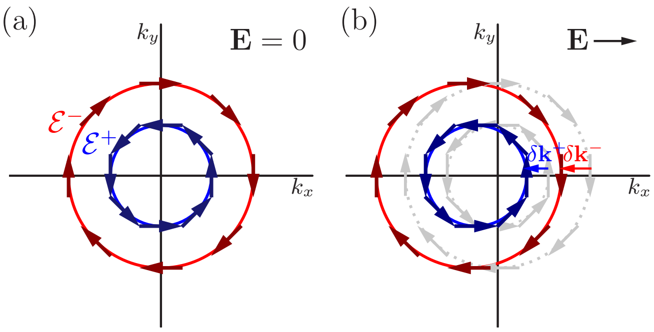

FIG. 2. Fermi lines ($\mathcal{E}_{\mathrm{F}} > 0$) with corresponding spin expectation values (arrows). Blue and red indicate the branch of the energy dispersion, $+$ or $-$. (a) In equilibrium, the total spin polarization vanishes. (b) If an external electric field $\vec{E} \parallel \vec{e}_x$ is applied, the Fermi lines are shifted opposite to the field direction, and a nonvanishing spin polarization perpendicular to $\vec{E}$ results.

Using the semiclassical Boltzmann transport theory [18], the influence of an external electric field $\vec{E}$ can be interpreted as a shift of the Fermi lines in $\vec{k}$ space by $\delta\vec{k}^{\nu} = -|e|\tau^{\nu}\vec{E}/\hbar$. Here, ν indicates the $+$ or $-$ branch, e is the elementary charge, and τ^{ν} is the transport lifetime. The shift of the Fermi lines is shown in Fig. 2(b).

Considering zero absolute temperature, the expectation value of the total spin is obtained as

$$\langle\vec{\sigma}\rangle = -\sum_{\vec{k},\nu} |e| \big(\vec{\Lambda}_{\vec{k}}^{\nu} \cdot \vec{E}\big) \delta[\mathcal{E}^{\nu}(\vec{k}) - \mathcal{E}_{\mathrm{F}}] \, \langle\vec{\sigma}\rangle_{\vec{k}}^{\nu} . \qquad (5)$$

Here, $\vec{\Lambda}_{\vec{k}}^{\nu}$ is the mean free path, and $\mathcal{E}_{\mathrm{F}}$ is the Fermi energy. Only states at the Fermi level contribute. The mean free path is approximated in the relaxation-time approximation, $\vec{\Lambda}_{\vec{k}}^{\nu} = \tau_{\vec{k}}^{\nu} \vec{v}_{\vec{k}}^{\nu}$, with the transport lifetime $\tau_{\vec{k}}^{\nu}$ and the group velocity $\vec{v}_{\vec{k}}^{\nu} = \frac{1}{\hbar}\nabla_{\vec{k}}\mathcal{E}^{\nu}(\vec{k})$.

For the calculation of the transport lifetime we consider scattering processes at δ-shaped scattering potentials placed at positions $\vec{R}_j$. The perturbation potential is $\Delta V(\vec{r}) = \sum_j U\delta(\vec{r} - \vec{R}_j)$, as proposed by Edelstein [2]. The impurity concentration is assumed to be small (dilute limit), so that the scattering potentials do not overlap. Considering a scattering event from an initial state $|\vec{k},\nu\rangle$ to a final state $|\vec{k}',\nu'\rangle$, the corresponding transition matrix $T_{\vec{k}'\leftarrow\vec{k}}^{\nu'\leftarrow\nu}$ is obtained in Born approximation, $T_{\vec{k}'\leftarrow\vec{k}}^{\nu'\leftarrow\nu} = \langle\vec{k}',\nu'|\Delta V|\vec{k},\nu\rangle$, where $|\vec{k},\nu\rangle$ are the unperturbed wave functions. The microscopic transition probability is given by Fermi's golden rule,

$$P_{\vec{k}'\leftarrow\vec{k}}^{\nu'\leftarrow\nu} = \frac{2\pi}{\hbar} c_{\mathrm{i}} N \big| T_{\vec{k}'\leftarrow\vec{k}}^{\nu'\leftarrow\nu} \big|^2 \delta[\mathcal{E}^{\nu}(\vec{k}) - \mathcal{E}^{\nu'}(\vec{k}')]. \qquad (6)$$

It is proportional to the impurity concentration c_{i} and the total number of atoms N. The transport lifetime $\tau_{\vec{k}}^{\nu}$ is obtained by the solution of the linearized Boltzmann equation [18]

$$\vec{v}_{\vec{k}}^{\nu} = \sum_{\vec{k}',\nu'} \big(P_{\vec{k}'\leftarrow\vec{k}}^{\nu'\leftarrow\nu} \tau_{\vec{k}}^{\nu} \vec{v}_{\vec{k}}^{\nu} - P_{\vec{k}\leftarrow\vec{k}'}^{\nu\leftarrow\nu'} \tau_{\vec{k}'}^{\nu'} \vec{v}_{\vec{k}'}^{\nu'} \big). \qquad (7)$$

With this theoretical background the spin density generated by the electric field $\vec{E}$ can be calculated. Usually, region II of Fermi energies above the Dirac point, $\mathcal{E}_{\mathrm{F}} > 0$, is discussed

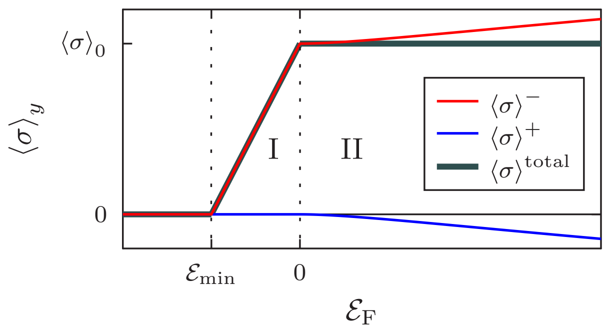

FIG. 3. Expectation value of the total spin $\langle\sigma\rangle^{\text{total}}$ (gray) versus Fermi energy $\mathcal{E}_{\text{F}}$. The contributions of the + and − branches are shown in blue and red, respectively. Above the Dirac point (region II), the expectation value of the total spin is constant with respect to $\mathcal{E}_{\text{F}}$, $\langle\sigma\rangle_0 = \frac{|e|\alpha_{\text{R}} N}{\pi c_{\text{i}}|U|^2}|\vec{E}|$. For Fermi energies between the band edge and the Dirac point, $\mathcal{E}_{\text{min}} < \mathcal{E}_{\text{F}} < 0$ (region I), the total spin increases linearly.

[2,3]. For those energies, both branches are occupied, and the spin expectation value per area A of the whole system is

$$\frac{\langle\vec{\sigma}\rangle}{A} = \frac{|e|}{4\pi\hbar}(\tau_{\text{F}}^- k_{\text{F}}^- - \tau_{\text{F}}^+ k_{\text{F}}^+)[\vec{e}_z \times \vec{E}]$$
$$= \frac{|e|\alpha_{\text{R}}}{\pi c_{\text{i}}|U|^2 A_0}[\vec{e}_z \times \vec{E}]. \tag{8}$$

Here, the index F indicates that the corresponding quantity is at the Fermi level. A_0 is the area of the unit cell.

The spin expectation values resulting from the two circles of the Fermi line point in opposite directions; thus, their contributions compensate partially. Due to the larger radius of the outer circle (−) a nonvanishing in-plane spin density remains which is perpendicular to the applied electric field, proportional to α_{R} and $|\vec{E}|$, and does not depend on the Fermi energy.

In addition to this usually considered energy range (region II) we also address region I below the Dirac point [21,22,27], $\mathcal{E}_{\text{min}} < \mathcal{E}_{\text{F}} < 0$. Here, only the − branch of the energy spectrum is occupied. The Fermi line consists of two concentric circles (denoted a and b); the occupied states are in between. As a result, the expectation value of the total spin density reads

$$\frac{\langle\vec{\sigma}\rangle}{A} = \frac{|e|}{4\hbar\pi}(\tau_{\text{a}}^- k_{\text{F,a}}^- - \tau_{\text{b}}^- k_{\text{F,b}}^-)$$
$$= \frac{|e|}{\pi c_{\text{i}}|U|^2 A_0}\left(\alpha_{\text{R}} + \frac{2\hbar^2}{\alpha_{\text{R}} m}\mathcal{E}_{\text{F}}\right)[\vec{e}_z \times \vec{E}]. \tag{9}$$

The spin density increases linearly with the Fermi energy from $\langle\vec{\sigma}\rangle = 0$ at the band edge ($\mathcal{E}_{\text{F}} = \mathcal{E}_{\text{min}} = -\frac{\alpha_{\text{R}}^2 m}{2\hbar^2}$) to $\langle\vec{\sigma}\rangle = \frac{|e|\alpha_{\text{R}} N_{\text{at}}}{\pi c|U|^2}[\vec{e}_z \times \vec{E}]$ at the Dirac point ($\mathcal{E}_{\text{F}} = 0$). Although both Fermi circles have identical spin textures, their contributions to the total spin compensate partially because the group velocity has opposite signs on the two circles, and therefore, the two Fermi circles are shifted in opposite directions. With decreasing Fermi energy the difference of the radii of the two circles gets smaller, which explains the linear energy dependence (Fig. 3).

In the calculation of the current-induced spin density from Eqs. (8) and (9) the impurity concentration c_{i} and the scattering potential U appear as parameters. If those quantities are not known, the spin density can be calculated depending on the two-dimensional charge current density $\vec{j}_{\text{c}}$. Within the Boltzmann transport theory, $\vec{j}_{\text{c}}$ is given by

$$\vec{j}_{\text{c}} = \frac{|e|^2}{A}\sum_{\vec{k},\nu}(\vec{\Lambda}_{\vec{k}}^{\nu}\cdot\vec{E})\delta[\mathcal{E}^{\nu}(\vec{k}) - \mathcal{E}_{\text{F}}]\vec{v}_{\vec{k}}^{\nu}\,, \tag{10}$$

which leads to the relation

$$\frac{\langle\vec{\sigma}\rangle}{A} = \frac{\alpha_{\text{R}} m\hbar}{|e|\left(\alpha_{\text{R}}^2 m + \hbar^2\mathcal{E}_{\text{F}}\right)}[\vec{e}_z \times \vec{j}_{\text{c}}] \tag{11}$$

for isotropic systems.

In this model, the 2DEG is confined to a plane with zero width (xy plane); hence, the scattering centers are located within that plane. At surfaces, the 2DEG's wave functions decay exponentially toward the bulk. Therefore, the overlap of these wave functions and the impurities depends on the position of the impurities, more precisely, on the distance from the surface. The less overlap there is, the smaller the scattering is, and the larger the transport lifetimes are [28,29]. This would enhance the ALGE effect. Put differently, our model simulates the maximum overlap of wave functions and scattering potentials. As assumed by Edelstein [2] and in this work, the impurity potentials are δ shaped. In real samples, however, the perturbation potentials are extended, or long range [30]. We note in passing that for extended potentials with a Gaussian shape (not reported here) the transition matrices (i.e., the overlap integral of initial and final wave functions with the perturbation potential) are reduced in comparison to δ-shaped impurities. As a consequence, the transport lifetime and the ALGE effect are increased. We recall that we take the dilute limit in which scattering potentials do not overlap. The semiclassical Boltzmann approach used here has the advantage that it provides a clear and comprehensive understanding of the physics of the ALGE effect. The number of parameters in the model is small due to the approximations made. For example, long-range potentials would introduce additional parameters, thereby increasing the computational effort but reducing the transparency. In this paper, we restrict ourselves to δ-shaped potentials; a treatment of realistic perturbation potentials is left to first-principles calculations [31,32].

In Table I the current-induced spin density for the Au(111) and Ag(111) surface states (sf) for an InGaAs/InAlAs heterostructure (hs) and the ordered $(\sqrt{3}\times\sqrt{3})R30^\circ$ Bi/Ag(111) surface alloy (sfal) is presented, calculated for $j_{\text{c}} = 10\,\text{A}\,\text{m}^{-1}$ within the isotropic model discussed above. Detailed insight into the microscopic origin of the band splitting of surface states is given in Ref. [33]. The Au(111) surface is often considered as a paradigm of a Rashba system [34,35]. However, it has been found that its surface states deviate from those of an ideal Rashba model with respect to the band structure at elevated energies and the spin-flip response to oscillating electric fields [36]. Since we consider energies close to the band crossing and the linear response to a time-independent electric field, these deviations are small, and Au(111) can safely be treated within the isotropic Rashba model.

TABLE I. Current-induced spin density $\langle\sigma\rangle_y/A$ for isotropic Rashba systems; sf = surface state, hs = heterostructure, sfal = surface alloy. Here, the two-dimensional current density is set to $j_{\mathrm{c}} = 10\,\mathrm{A\,m^{-1}}$ in the x direction. The parameters m, α_{R}, and $\mathcal{E}_{\mathrm{F}}$ are taken from the cited references; m_{e} is the electron mass.

System	m (units of m_{e})	α_{R} (eV Å)	$\mathcal{E}_{\mathrm{F}}$ (eV)	$\langle\sigma\rangle_y/A$ ($10^8\,\mathrm{cm}^{-2}$)	Reference
Au(111) sf	0.27	0.33	0.475	10.03	[34], [37]
Ag(111) sf	0.37	0.03	0.178	3.36	[37], [38]
InGaAs/InAlAs hs	0.05	0.07	0.092	2.05	[39]
Bi/Ag(111) sfal	−0.35	3.05	−0.180	94.77	[14], [23]

The strong Rashba splitting of the Au(111) surface states leads to a sizable ALGE effect. In contrast, the current-induced spin density of the Ag(111) surface states and the InGaAs/InAlAs heterostructure are smaller by a factor of 1/3 and 1/5, respectively, compared with Au(111). This is explained by the remarkably smaller Rashba splitting of Ag(111) and InGaAs/InAlAs, which is the main reason for the reduced ALGE effect. The Bi/Ag(111) surface alloy has a "giant" Rashba splitting which is mainly caused by an additional in-plane potential gradient [23]. However, the Fermi energy of this system is outside this band with the giant spin splitting [23]. In order to calculate the current-induced spin density for this system, the Fermi energy was deliberately assumed within the strongly split band here. Consequently, a remarkably large total spin density is induced.

B. Anisotropic systems

The isotropic free-electron model is not suitable for systems with an anisotropic energy dispersion. Using a $\vec{k}\cdot\vec{p}$ approach [40], the Hamiltonian of Eq. (1) can be modified to obtain an appropriate description of systems of reduced symmetry.

1. $C_{2\mathrm{v}}$ symmetry

For systems with $C_{2\mathrm{v}}$ symmetry, such as the (110) surface of an fcc crystal, an anisotropy of the effective mass m and the Rashba parameter α_{R} are introduced, $m_x \neq m_y$ and $\alpha_{\mathrm{R}x} \neq \alpha_{\mathrm{R}y}$, where x and y correspond to the directions of the symmetry axes. Then, the Hamiltonian (1) reads [40,41]

$$\hat{H} = \frac{\hbar^2 k_x^2}{2m_x} + \frac{\hbar^2 k_y^2}{2m_y} + \alpha_{\mathrm{R}x}k_x\hat{\sigma}_y - \alpha_{\mathrm{R}y}k_y\hat{\sigma}_x. \tag{12}$$

The energy eigenvalues are

$$\mathcal{E}^{\pm}(\vec{k}) = \frac{\hbar^2 k_x^2}{2m_x} + \frac{\hbar^2 k_y^2}{2m_y} \pm \sqrt{\alpha_{\mathrm{R}x}^2 k_x^2 + \alpha_{\mathrm{R}y}^2 k_y^2}. \tag{13}$$

Thus, the position of the band edge and the band curvature are anisotropic, as shown in Figs. 4(a) and 4(b) for a characteristic system ($m_x = 0.5m_y$, $\alpha_{\mathrm{R}x} = \alpha_{\mathrm{R}y}$), which will be discussed exemplary in the following. We distinguish three energy regions. In region II, $\mathcal{E}_{\mathrm{F}} > 0$, both the + and − branches are occupied. At $\mathcal{E}_{\mathrm{F}} = \mathcal{E}_{\mathrm{S}} = -1/2\hbar^2 \min(\alpha_{\mathrm{R}x}^2 m_x, \alpha_{\mathrm{R}y}^2 m_y)$ the band edge is reached in one $\vec{k}$ direction, either k_x or k_y. Here, saddle points with the energy $\mathcal{E}_{\mathrm{S}}$ separate the energy regions Ib ($\mathcal{E}_{\mathrm{S}} < \mathcal{E}_{\mathrm{F}} < 0$) and Ia ($\mathcal{E}_{\mathrm{min}} < \mathcal{E}_{\mathrm{F}} < \mathcal{E}_{\mathrm{S}}$).

In Figs. 4(c)–4(f) Fermi lines ($m_x = 0.5m_y, \alpha_{\mathrm{R}x} = \alpha_{\mathrm{R}y}$) are shown for selected Fermi energies $\mathcal{E}_{\mathrm{F}}$. In energy region II they are closed concentric curves, as shown in Fig. 4(c). Directly below the Dirac point (Ib) the Fermi line consists of two closed concentric curves originating from the − branch, depicted in Fig. 4(d). For $\mathcal{E}_{\mathrm{F}} = \mathcal{E}_{\mathrm{S}}$ van Hove singularities of the density of states exist [42]. At the saddle points the Fermi lines intersect, as shown in Fig. 4(e). In energy range Ia not all directions of the $\vec{k}$ space are occupied; the Fermi lines consist of two separated closed curves which reduce to two points at the band edge, depicted in Fig. 4(f). This change of the topology of the Fermi lines is a Lifshitz transition [43].

Due to the asymmetry of the Rashba parameters, the $\vec{k}$-dependent spin expectation values are not always perpendicular to $\vec{k}$ but rotated within the plane favoring the direction of the symmetry axis with the smaller Rashba parameter,

$$\langle\vec{\sigma}\rangle^{\pm}_{\vec{k}} = \pm\frac{1}{\tilde{k}^{\pm}}(\vec{e}_z \times \vec{\tilde{k}}^{\pm}), \tag{14}$$

where $\vec{\tilde{k}} = (\alpha_{\mathrm{R}x}k_x, \alpha_{\mathrm{R}y}k_y)$. In Figs. 4(c)–4(f) $\langle\vec{\sigma}\rangle^{\pm}_{\vec{k}}$ is sketched for the energy regions discussed above.

The expectation value of the total spin is calculated numerically using Eq. (5) due to the anisotropy of the system. We use an adaptive triangle method to determine the $\vec{k}$ points of the Fermi line and perform a numerical integration using linear interpolation. This procedure is presented in the Appendix.

In Fig. 5 the current-induced ALGE total spin $\langle\sigma\rangle_y$ versus the Fermi energy is shown. The data are representative of systems which pass through a Lifshitz transition.

In energy region II the current-induced total spin is nearly constant but increases weakly with the Fermi energy. For $\mathcal{E}_{\mathrm{S}} < \mathcal{E}_{\mathrm{F}} < 0$ (Ib) the total spin depends almost linearly on the Fermi energy. Around $\mathcal{E}_{\mathrm{S}}$ strong deviations from the quasilinearity occur; at $\mathcal{E}_{\mathrm{F}} = \mathcal{E}_{\mathrm{S}}$ it is even reduced to zero. This reduction can be understood by a closer inspection of the mean free path on the Fermi lines, $\vec{\Lambda}^{-}_{\vec{k}} = \vec{v}^{-}_{\vec{k}}\tau^{-}_{\vec{k}}$. In $\vec{k}$ space the Fermi lines intersect at the saddle points. Here, the group velocity is zero. The linearized Boltzmann equation (7) leads to a vanishing transport lifetime for all $\vec{k}$ points of the Fermi line apart from the saddle points. Thus, the mean free path $\vec{\Lambda}_{\vec{k}}$ is zero for the whole Fermi line, and the total spin vanishes. For Fermi energies below this saddle point (region Ia) not all directions of the $\vec{k}$ space are occupied. Here, the total spin expectation value depends nearly linearly on $\mathcal{E}_{\mathrm{F}}$ and is reduced to zero at the band edge. Due to the modified shape of the Fermi lines the slope of $\langle\sigma\rangle_y$ is smaller than in region Ib.

An example of a Rashba system with $C_{2\mathrm{v}}$ symmetry is the surface states of Au(110), described by the parameters $m_x = 0.11m_{\mathrm{e}}$, $m_y = 0.32m_{\mathrm{e}}$, $\alpha_{\mathrm{R}x} = 0.80\,\mathrm{eV\,Å}$, $\alpha_{\mathrm{R}y} = 0.17\,\mathrm{eV\,Å}$

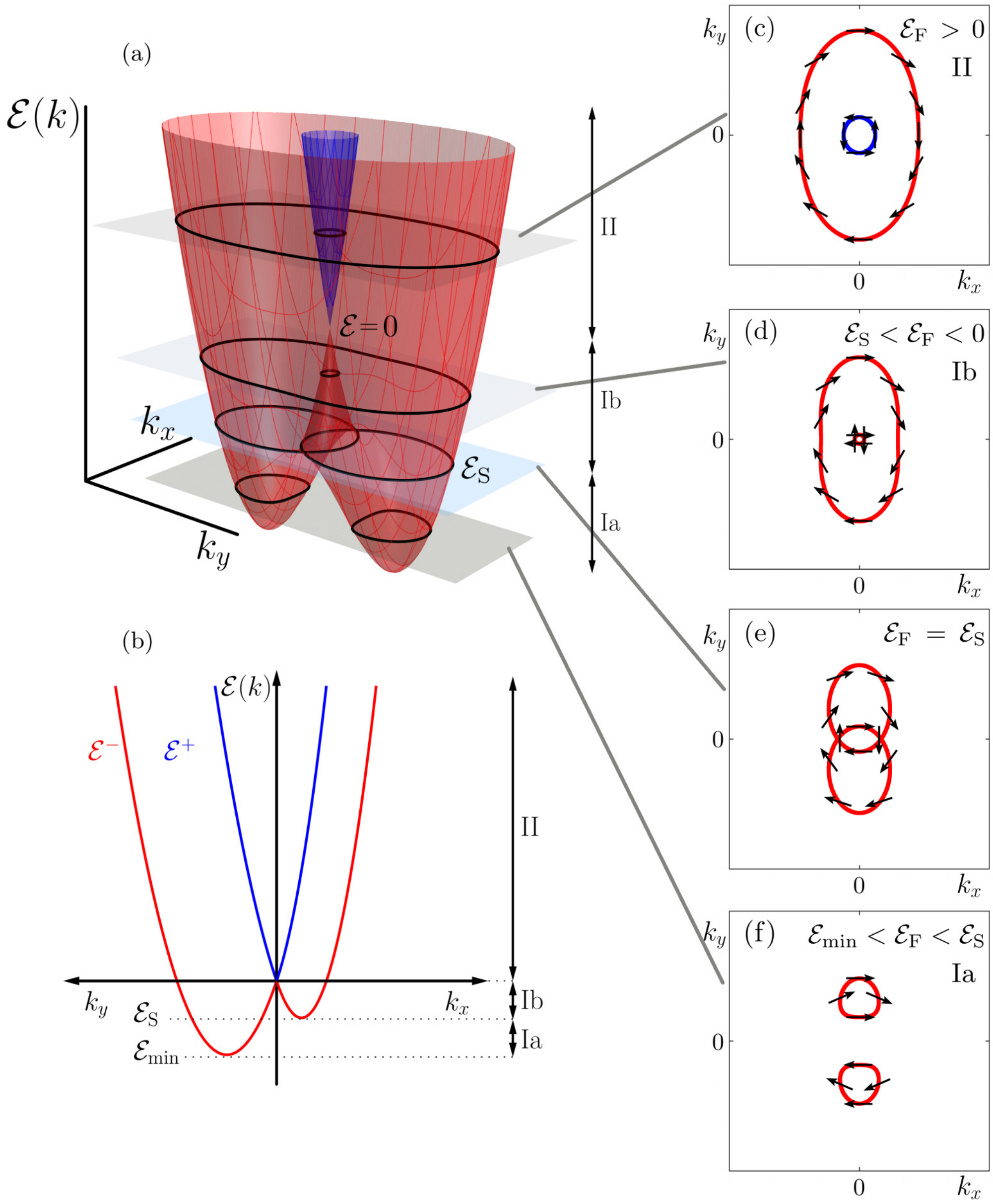

FIG. 4. (a) Energy dispersion of a Rashba system with $C_{2\mathrm{v}}$ symmetry ($m_x = 0.5m_y$, $\alpha_{\mathrm{R}x} = \alpha_{\mathrm{R}y}$) in two-dimensional $\vec{k}$ space (schematic). (b) In addition, the energy spectrum is shown for the k_x and k_y directions. At $\mathcal{E}_\mathrm{S}$ the band minimum in one direction (here, the k_x direction) is reached, and a saddle point occurs. (c)–(f) The Fermi lines for selected energies; the arrows represent the direction of the spin expectation value $\langle\vec{\sigma}\rangle^{\pm}_{\vec{k}}$.

(Ref. [41]); x and y correspond to the crystallographic directions [001] and [$\bar{1}$10], respectively. In Table II the current-induced spin density of Au(110) surface states is presented. The spin density is calculated for an electric field in the directions of the main symmetry axes, [001] and [$\bar{1}$10]. Here, the absolute value of $\vec{E}$ is set constant and corresponds to a field which produces a two-dimensional charge current density of 10 A m^{-1} if it is applied in the [001] direction. Obviously, the absolute value of the spin density strongly depends on the direction of the electric field. If the electric field is in the [001] direction, $\langle\sigma\rangle$ is enhanced by more than 100% in comparison to the spin density induced by an electric field in the [$\bar{1}$10] direction.

TABLE II. Current-induced spin density of Au(110) surface states. The model parameters $m_x = 0.11m_\mathrm{e}$, $m_y = 0.32m_\mathrm{e}$, $\alpha_{\mathrm{R}x} = 0.80\,\mathrm{eV\,Å}$, $\alpha_{\mathrm{R}y} = 0.17\,\mathrm{eV\,Å}$, $\mathcal{E}_\mathrm{F} = 0.370\,\mathrm{eV}$ are taken from Ref. [41]. The absolute value of the electric field corresponds to the field which induces a two-dimensional charge current density of 10 A m^{-1} if it is applied in the [001] direction.

Direction of $\vec{E}$	j_c(A m^{-1})	$\langle\sigma\rangle/A$ (10^8 cm^{-2})
$\vec{E} \parallel [001] \parallel x$	10.00(j_x)	8.53($\langle\sigma\rangle_y/A$)
$\vec{E} \parallel [\bar{1}10] \parallel y$	3.48(j_y)	−3.59($\langle\sigma\rangle_x/A$)

To gain a better understanding of the influence of the anisotropy of the effective mass and the Rashba parameter we consider the anisotropy of both quantities separately. First,

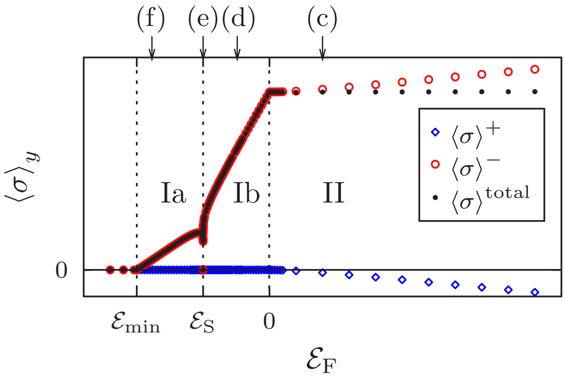

FIG. 5. Total spin expectation value of a system with C_{2v} symmetry ($m_x = 0.5m_y$, $\alpha_{Rx} = \alpha_{Ry}$). The external electric field is applied in the x direction. The contributions of the + and − branches are shown in blue and red, respectively. The selected energies for which the Fermi lines are sketched in Figs. 4(c)–4(f) are marked by arrows.

we assume $\alpha_{Rx} = \alpha_{Ry}$ and $m_x \neq m_y$. The mass anisotropy generates anisotropic Fermi lines. The absolute value of the Fermi vector is largest in the direction of the larger effective mass [for Au(110): $[\bar{1}10]$ direction]. If the electric field is applied in this direction, the Fermi lines are shifted in the opposite field direction, which implies that, mainly, states at the less extended side of the Fermi line contribute to the spin density. If the electric field is applied in the direction with the smaller effective mass [for Au(110): [001]], the Fermi lines are shifted in such a manner that, mainly, the states at the elongated side of the Fermi lines contribute to the spin density. Therefore, in general a larger total spin density is expected if the electric field is applied in the direction of the smaller effective mass.

Now, $m_x = m_y$ and $\alpha_{Rx} \neq \alpha_{Ry}$ are assumed. The anisotropy of the Rashba parameter also affects the symmetry of the Fermi line. In addition, the $\vec{k}$-dependent spin expectation values on the Fermi lines are rotated in the direction of the smaller Rashba parameter, as expressed by Eq. (14). For reasons of symmetry the total spin polarization in the direction of $\vec{E}$ is always zero, and only a total spin perpendicular to $\vec{E}$ remains. This field-induced spin density is large if $\langle\vec{\sigma}\rangle^{\pm}_{\vec{k}}$ have large components perpendicular to $\vec{E}$. This means that the total spin density is larger if $\vec{E}$ is applied in the direction with the larger Rashba parameter [for Au(110) surface states: [001] direction].

These considerations explain qualitatively the orientation dependence of the ALGE effect in Au(110) surface states, given in Table II. In general, for systems with C_{2v} symmetry the ALGE effect can be enhanced by an appropriate choice of the direction of $\vec{E}$.

The bulk inversion asymmetry in noncentrosymmetric crystals (e.g., zinc blende) leads to a Dresselhaus SOC contribution which depends on the crystal growth direction [44]. Like the Rashba term, the Dresselhaus term in the Hamiltonian produces spin splitting. Depending on the point-group symmetry of the system and the ratio of Rashba and Dresselhaus SOC, unconventional spin textures show up, for example, in systems with a single spin component [45] or showing a persistent spin helix [46].

Due to the symmetry breaking caused by the Dresselhaus SOC, current-induced spin polarization is expected [20,47]. In such systems, the ALGE effect can be analyzed as in Rashba systems. If the Hamiltonian depends only on one spin component [45] the spin expectation values are constant on both energy branches and do not depend on $\vec{k}$. As a result, an electric field does not induce a finite spin density for symmetry reasons. If the Rashba and the linear in-plane Dresselhaus term are of the same strength, a persistent spin helix occurs in real space [46]. The spin expectation values on the Fermi lines are parallel but point in opposite directions within one energy branch [3]. Therefore, a nonvanishing spin density is expected whose orientation does not depend on the direction of $\vec{E}$. Its absolute value reaches a maximum for $\vec{E}$ pointing in the direction of constant spin in real space and is minimized when $\vec{E}$ is oriented perpendicular.

2. C_{3v} symmetry

For systems with C_{3v} symmetry, such as fcc (111) surface states and ordered (111) surface alloys, an additional in-plane potential gradient occurs due to the in-plane structural inversion asymmetry [23]. The corresponding Hamiltonian contains an additional term proportional to $\hat{\sigma}_z$ and third order in k [26],

$$\hat{H} = \frac{\hbar^2\vec{k}^2}{2m} + \alpha_{\text{R}}(k_x\hat{\sigma}_y - k_y\hat{\sigma}_x) + \frac{\lambda}{2}(k_+^3 + k_-^3)\hat{\sigma}_z\,, \tag{15}$$

where the parameter λ characterizes the strength of the in-plane gradient and $k_\pm \equiv k_x \pm ik_y$. Here, one mirror plane was chosen to be in the k_y direction. Ast *et al.* [23] and Premper *et al.* [24] have shown that such an in-plane potential gradient, e.g., in the Ag/Bi($\sqrt{3} \times \sqrt{3}$)$R30^\circ$ surface alloy, results in a strongly enhanced spin splitting. Therefore, those systems are expected to provide a large ALGE effect. The energy eigenvalues of the Hamiltonian (15) are

$$\mathcal{E}^{\pm}(\vec{k}) = \frac{\hbar^2k^2}{2m} \pm \sqrt{\alpha_{\text{R}}^2k^2 + \lambda^2k^6\cos^2(3\varphi_{\vec{k}})}. \tag{16}$$

This energy spectrum has sixfold rotational symmetry. In the directions of the mirror planes the band structure is unchanged with respect to the isotropic model, whereas the influence of the term $\lambda^2k^6\cos^2(3\varphi_{\vec{k}})$ is maximal in the directions perpendicular to three mirror planes [48]. The additional third-order Hamiltonian, $\hat{H}_3 = \lambda/2(k_+^3 + k_-^3)\hat{\sigma}_z$, also called the warping term, mainly affects the states with large absolute values of k, which lie on the − branch.

In Fig. 6 the Fermi lines of a system with C_{3v} symmetry are shown. The outer line (−) has a hexagonal warped shape; the inner line (+) is nearly circular.

Due to the in-plane potential gradient the $\vec{k}$-dependent spin expectation values $\langle\vec{\sigma}\rangle_{\vec{k}}$ contain an out-of-plane component which increases with λ. This component is maximal at the regions of the Fermi lines which deviate most from the isotropic case, as sketched in Fig. 6.

The ALGE effect is calculated as for C_{2v} symmetry. In Table III the current-induced spin density for the Bi/Cu(111) and Bi/Ag(111) ($\sqrt{3} \times \sqrt{3}$)$R30^\circ$ surface alloys is shown. To illustrate the influence of the additional warping term of the

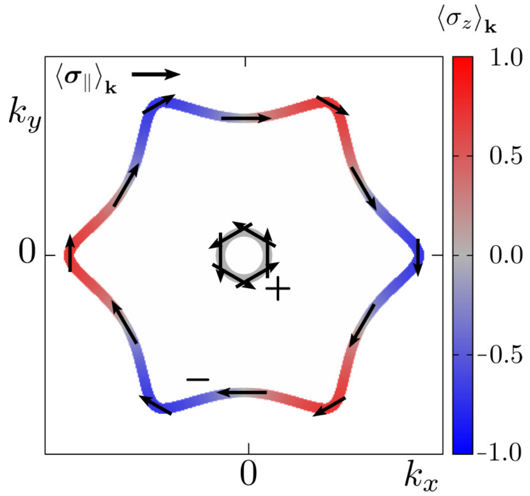

FIG. 6. Fermi lines of a system with $C_{3\mathrm{v}}$ symmetry and $\mathcal{E}_\mathrm{F} > 0$ ($m = m_\mathrm{e}$, $\alpha_\mathrm{R} = 1$ eV Å and $\lambda = 5.8$ eV Å^3). The inner line corresponds to the + branch; the outer corresponds to the − branch. The arrows illustrate the in-plane component of the spin expectation value; the color scale indicates the out-of-plane component.

Hamiltonian (15), the spin density was calculated without ($\lambda = 0$) and with ($\lambda \neq 0$) this term.

For both systems the additional third-order term reduces the expectation value of the total spin density in comparison to the isotropic model ($\lambda = 0$).

With increasing λ the $\vec{k}$-dependent spin expectation values are rotated out of the plane, as shown in Fig. 6; this reduces the in-plane component of $\langle\vec{\sigma}\rangle_{\vec{k}}$, leading to a decreased current-induced in-plane spin density. For symmetry reasons the total spin is completely in plane. In addition, the deviations of the Fermi lines from the circular shape cause a further reduction of the spin density.

C. Topological insulators

Besides the Rashba systems, a current-induced spin polarization is also expected in the surface states of three-dimensional topological insulators [25]. As in Rashba systems, spin and momentum are coupled, and the spin texture is helical. Whereas in Rashba systems the Fermi lines consist of two curves whose contributions to the ALGE effect compensate partially, the surface states of topological insulators provide a single Fermi circle. Therefore, an enhanced ALGE effect is expected in topological insulators.

TABLE IV. Current-induced spin density $\langle\sigma\rangle_y/A$ for the surface states of selected topological insulators. The two-dimensional current density is set to $\vec{j}_\mathrm{c} = 10\,\mathrm{A\,m^{-1}}\,\vec{e}_x$. Here, results for isotropic systems and for systems with hexagonal warping are presented.

System	v_F ($10^5\,\mathrm{m\,s^{-1}}$)	λ (eV Å^3)	$\mathcal{E}_\mathrm{F}$ (eV)	$\langle\sigma\rangle_y/A$ ($10^8\,\mathrm{cm^{-2}}$)	Reference
α-Sn	6.0	0	0.50 · · · 0.85	−104.01	[25]
$\mathrm{Bi_2Se_3}$	6.2	0		−100.69	[52]
$\mathrm{Bi_2Se_3}$, Cu doped	2.9	140	0.45	−22.11	[48]
$\mathrm{Bi_2Te_3}$, Sn doped	3.9	250	0.28	−71.08	[26]

The Hamiltonian

$$\hat{H} = \hbar v_\mathrm{F}(k_x\hat{\sigma}_y - k_y\hat{\sigma}_x) \tag{17}$$

yields the linear energy dispersion

$$\mathcal{E}^\pm(k) = \pm\hbar v_\mathrm{F} k\ , \tag{18}$$

where v_F is the Fermi velocity. The Dirac point is at $\mathcal{E} = 0$; the energy range above (below) the Dirac point is described by the + (−) branch of the energy spectrum (18). The whole energy range is not degenerate except for the Dirac point. The spin density induced by an electric field $\vec{E}$ reads

$$\frac{\langle\vec{\sigma}\rangle}{A} = \frac{-|e|}{4\pi\hbar}\tau_\mathrm{F}k_\mathrm{F}[\vec{e}_z \times \vec{E}] = \frac{-|e|\hbar v_\mathrm{F}}{\pi c_\mathrm{i}|U|^2 A_0}[\vec{e}_z \times \vec{E}]. \tag{19}$$

This result differs from the expression for the isotropic Rashba systems with $\mathcal{E}_\mathrm{F} > 0$ (8) only by the sign and a factor of $\hbar v_\mathrm{F}$ instead of α_R. The total spin density is constant within the whole energy range, except for the Dirac point, at which the model is not applicable. For states with opposite chirality the spin density has opposite signs. Therefore, by measuring the sign of the spin density generated by the ALGE effect the chirality of the surface states of topological insulators can be determined directly.

For topological insulators with $C_{3\mathrm{v}}$ symmetry at the surface, the isotropic Hamiltonian (17) is modified by an additional third-order warping term $\lambda/2(k_+^3 + k_-^3)\hat{\sigma}_z$ (Ref. [26]), as in Eq. (15).

In Table IV the spin density in topological insulators generated by a two-dimensional charge current, $j_\mathrm{c} = 10\,\mathrm{A\,m^{-1}}$, is shown. The α-Sn and $\mathrm{Bi_2Se_3}$ surface states are approximated within the isotropic model; for the surface states of Cu-doped $\mathrm{Bi_2Se_3}$ and Sn-doped $\mathrm{Bi_2Te_3}$ the warping term of the Hamiltonian is included. In general, the absolute values of the

TABLE III. Current-induced spin density $\langle\sigma\rangle_y/A$ for Bi/Cu(111) and Bi/Ag(111) $(\sqrt{3}\times\sqrt{3})R30^\circ$ surface alloys. The two-dimensional current density is set constant to $j_\mathrm{c} = 10\,\mathrm{A\,m^{-1}}$ in the x direction. The spin density $\langle\sigma\rangle_y$ is calculated without ($\lambda = 0$) and with ($\lambda \neq 0$) the warping term. As in Table I, the Fermi energy of the Bi/Ag surface alloy was assumed within the band with strong Rashba SOC.

System	m (units of m_e)	α_R (eV Å)	λ (eV Å^3)	$\mathcal{E}_\mathrm{F}$ (eV)	$\langle\sigma\rangle_y/A$ ($10^8\,\mathrm{cm^{-2}}$)	References
Bi/Cu(111)	−0.29	0.85	0	−0.215	54.78	[48–50]
			12		50.30	
Bi/Ag(111)	−0.32	2.95	0	−0.180	93.30	[14,23,48,49,51]
			18		89.22	

spin density are larger than for the isotropic Rashba systems presented in Table I. For the topological insulators considered here the product $\hbar v_{\mathrm{F}}$ is in the range from 1.91 to 4.08 eV Å, which is large in comparison to the Rashba parameter α_{R} of the Rashba systems in Table I.

One could argue that the enhanced ALGE effect is caused mainly by the large factor of $\hbar v_{\mathrm{F}}$ in comparison to α_{R} since the analytical expressions (8) and (19) are very similar. However, the models discussed here describe qualitatively different physical systems. For a comparison between Rashba systems and topological insulators a more detailed consideration is needed.

For small k the Rashba Hamiltonian (1) is approximated in first order in k by the Hamiltonian (17), which is used for topological insulators. Within this approximation, the Fermi circle of a topological insulator corresponds to the inner Fermi circle of a Rashba system. However, the current-induced spin density in a topological insulator is not equivalent to the contribution of the inner Fermi circle of a Rashba system since in topological insulators only scattering events within the single Fermi circle contribute to the transport lifetime, whereas in Rashba systems intercircle scattering is also considered. Therefore, the spin density in topological insulators does not depend on the Fermi energy, while the contribution of the inner Fermi line of Rashba systems shows an energy dependence. Hence, the similarity of the analytic expressions (8) and (19) is by chance rather than of physical origin.

III. CONCLUSION

We provide a complete framework for theoretical consideration of the ALGE effect in common two-dimensional systems. Using the semiclassical Boltzmann transport theory, we present a model for the calculation of the ALGE effect in isotropic and anisotropic Rashba systems as well as in topological insulators. In isotropic systems the total spin generated by an electric field is energy independent for Fermi energies above the Dirac point but increases linearly with the Fermi energy between the band edge and the Dirac point. By introducing anisotropic effective masses and Rashba parameters the isotropic Rashba model can be expanded to anisotropic systems with $C_{2\mathrm{v}}$ symmetry. When saddle points of the dispersion occur and the Fermi contours pass through a Lifshitz transition, the total spin of the system vanishes. The ALGE effect can be enhanced by an appropriate choice of the electric field direction (in the direction of smaller effective mass and larger Rashba parameter). For systems with $C_{3\mathrm{v}}$ symmetry we include an additional in-plane potential gradient. The consideration of this gradient reduces the calculated spin density slightly; on the other hand, it leads to an enormous Rashba parameter which enhances the ALGE effect. In topological insulators a comparably large ALGE effect is expected since here only one Fermi circle exists; thus no partial compensation of contributions from other Fermi circles occurs. The sign of the current-induced spin density in topological insulators is determined by the chirality. The ALGE effect provides an opportunity to measure the chirality directly.

Our findings call for experimental verification, especially of the energy dependence, the reduction of the current-induced spin density at the Lifshitz transition, and the influence of the electric field direction. In addition, this work may motivate an *ab initio* treatment of the ALGE effect.

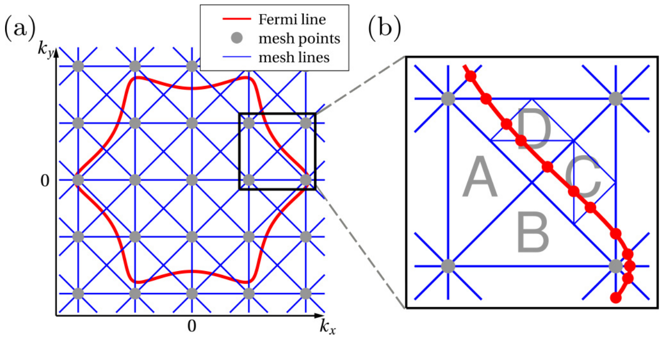

FIG. 7. Adaptive triangle method for the determination of the Fermi lines. (a) The $\vec{k}$ space is divided by a rectangular mesh (gray dots). The mesh points are connected in such a way that triangles are formed (blue lines). The red line is a complex Fermi line. (b) Detail of (a). To determine the $\vec{k}$ points on the Fermi line (red dots) an adaptive procedure is used. Triangles A and B are not intersected by the Fermi line; therefore, they are not considered further. The Fermi line passes through triangles C and D; they are divided iteratively into smaller triangles until the required precision is reached.

ACKNOWLEDGMENTS

We thank D. V. Fedorov for useful discussions. This work was supported by the Deutsche Forschungsgemeinschaft via SPP 1666.

APPENDIX: NUMERICAL ASPECTS

If the shape of the Fermi contours deviates from a circle or an ellipse, a parametrization for integration along the Fermi lines is usually not possible. Therefore, we use numerical methods for the determination of the Fermi lines, the integration along the curves, and the solution of the linearized Boltzmann equation (7). In the following, the basic ideas of this numerical procedure are outlined.

First, the $\vec{k}$ points of the Fermi lines need to be determined. We use an adaptive triangle method [53] which is sketched schematically in Fig. 7. The $\vec{k}$ space is divided by a rectangular grid. By connecting the grid points with straight lines, triangles are generated, as shown in Fig. 7(a). Now, for each triangular point (all points of the grid and the center of four grid points), the energy $\mathcal{E}(\vec{k})$ is calculated from Eqs. (13) and (16), respectively. If the Fermi line passes between two triangular points, then the function $\mathcal{E}(\vec{k}) - \mathcal{E}_{\mathrm{F}}$ must change sign in between those points. A triangle which is intersected by the Fermi line is divided into four smaller triangles with the centers of the edges as new points, as shown in Fig. 7(b). This procedure is repeated until the desired precision is reached. If none of the triangular edges intersects the Fermi line, the triangle is not considered further. This adaptive method requires only a coarse mesh in the regions without Fermi lines, whereas the sampling of the Fermi line is more precise.

For the summation in $\vec{k}$ space the sums of occupied states in $\vec{k}$ space are converted to integrations along the Fermi line as

$$\sum_{\vec{k}} \delta[\mathcal{E}(\vec{k}) - \mathcal{E}_{\mathrm{F}}] \rightarrow \frac{A}{(2\pi)^2\hbar} \int_{\vec{k}=\vec{k}_{\mathrm{F}}} \frac{1}{v_{\vec{k}}}\, dk_{\parallel}. \qquad \text{(A1)}$$

Those line integrals are solved numerically according to the trapezoidal rule,

$$\int_{\vec{k}=\vec{k}_{\mathrm{F}}} f(\vec{k}) dk_{\parallel} \approx \sum_{j=1}^{N_k} \frac{1}{2}[f(\vec{k}_j) + f(\vec{k}_{j+1})]|\vec{k}_j - \vec{k}_{j+1}|, \quad \text{(A2)}$$

where $f(\vec{k})$ is an arbitrary function and N_k is the number of $\vec{k}$ points which approximate the Fermi line.

The linearized Boltzmann equation (7) is transformed into a matrix equation and solved by LU decomposition [54].

---

[1] A. G. Aronov and Y. Lyanda-Geller, JETP Lett. **50**, 431 (1989).

[2] V. Edelstein, Solid State Commun. **73**, 233 (1990).

[3] P. Gambardella and I. M. Miron, Philos. Trans. R. Soc. A **369**, 3175 (2011).

[4] Y. Bychkov and E. I. Rashba, JETP Lett. **39**, 78 (1984).

[5] Y. A. Bychkov and E. I. Rashba, J. Phys. C **17**, 6039 (1984).

[6] E. Rashba, Sov. Phys. Solid State **2**, 1109 (1960).

[7] R. H. Silsbee, Phys. Rev. B **63**, 155305 (2001).

[8] R. H. Silsbee, J. Phys. Condens. Matter **16**, R179 (2004).

[9] J.-i. Inoue, G. E. W. Bauer, and L. W. Molenkamp, Phys. Rev. B **67**, 033104 (2003).

[10] K. Shen, G. Vignale, and R. Raimondi, Phys. Rev. Lett. **112**, 096601 (2014).

[11] Y. K. Kato, R. C. Myers, A. C. Gossard, and D. D. Awschalom, Phys. Rev. Lett. **93**, 176601 (2004).

[12] V. Sih, R. C. Myers, Y. K. Kato, W. H. Lau, A. C. Gossard, and D. D. Awschalom, Nat. Phys. **1**, 31 (2005).

[13] A. Y. Silov, P. A. Blajnov, J. H. Wolter, R. Hey, K. H. Ploog, and N. S. Averkiev, Appl. Phys. Lett. **85**, 5929 (2004).

[14] H. J. Zhang, S. Yamamoto, B. Gu, H. Li, M. Maekawa, Y. Fukaya, and A. Kawasuso, Phys. Rev. Lett. **114**, 166602 (2015).

[15] J. C. Rojas Sánchez, L. Vila, G. Desfonds, S. Gambarelli, J. P. Attané, J. M. De Teresa, C. Magén, and A. Fert, Nat. Commun. **4**, 2944 (2013).

[16] M. Isasa, M. C. Martínez-Velarte, E. Villamor, C. Magén, L. Morellón, J. M. De Teresa, M. R. Ibarra, G. Vignale, E. V. Chulkov, E. E. Krasovskii, L. E. Hueso, and F. Casanova, Phys. Rev. B **93**, 014420 (2016).

[17] S. Sangiao, J. M. De Teresa, L. Morellon, I. Lucas, M. C. Martinez-Velarte, and M. Viret, Appl. Phys. Lett. **106**, 172403 (2015).

[18] I. Mertig, Rep. Prog. Phys. **62**, 237 (1999).

[19] A. Manchon and S. Zhang, Phys. Rev. B **79**, 094422 (2009).

[20] M. Trushin and J. Schliemann, Phys. Rev. B **75**, 155323 (2007).

[21] C. Xiao, D. Li, and Z. Ma, Phys. Rev. B **93**, 075150 (2016).

[22] C. Xiao, D. Li, and Z. Ma, Front. Phys., **11**, 117201 (2016).

[23] C. R. Ast, J. Henk, A. Ernst, L. Moreschini, M. C. Falub, D. Pacilé, P. Bruno, K. Kern, and M. Grioni, Phys. Rev. Lett. **98**, 186807 (2007).

[24] J. Premper, M. Trautmann, J. Henk, and P. Bruno, Phys. Rev. B **76**, 073310 (2007).

[25] J.-C. Rojas-Sánchez, S. Oyarzún, Y. Fu, A. Marty, C. Vergnaud, S. Gambarelli, L. Vila, M. Jamet, Y. Ohtsubo, A. Taleb-Ibrahimi, P. Le Fèvre, F. Bertran, N. Reyren, J.-M. George, and A. Fert, Phys. Rev. Lett. **116**, 096602 (2016).

[26] L. Fu, Phys. Rev. Lett. **103**, 266801 (2009).

[27] A. Dyrdał, M. Inglot, V. K. Dugaev, and J. Barnaś, Phys. Rev. B **87**, 245309 (2013).

[28] P. Zahn, J. Binder, I. Mertig, R. Zeller, and P. H. Dederichs, Phys. Rev. Lett. **80**, 4309 (1998).

[29] C. Herschbach, M. Gradhand, D. V. Fedorov, and I. Mertig, Phys. Rev. B **85**, 195133 (2012).

[30] A. D. Mirlin, J. Wilke, F. Evers, D. G. Polyakov, and P. Wölfle, Phys. Rev. Lett. **83**, 2801 (1999).

[31] M. Gradhand, D. V. Fedorov, P. Zahn, and I. Mertig, Phys. Rev. B **81**, 245109 (2010).

[32] M. Gradhand, D. V. Fedorov, P. Zahn, and I. Mertig, Phys. Rev. Lett. **104**, 186403 (2010).

[33] E. E. Krasovskii, Phys. Rev. B **90**, 115434 (2014).

[34] S. LaShell, B. A. McDougall, and E. Jensen, Phys. Rev. Lett. **77**, 3419 (1996).

[35] M. Hoesch, M. Muntwiler, V. N. Petrov, M. Hengsberger, L. Patthey, M. Shi, M. Falub, T. Greber, and J. Osterwalder, Phys. Rev. B **69**, 241401 (2004).

[36] J. Ibañez-Azpiroz, A. Bergara, E. Y. Sherman, and A. Eiguren, Phys. Rev. B **88**, 125404 (2013).

[37] H. Cercellier, C. Didiot, Y. Fagot-Revurat, B. Kierren, L. Moreau, D. Malterre, and F. Reinert, Phys. Rev. B **73**, 195413 (2006).

[38] D. Popović, F. Reinert, S. Hüfner, V. G. Grigoryan, M. Springborg, H. Cercellier, Y. Fagot-Revurat, B. Kierren, and D. Malterre, Phys. Rev. B **72**, 045419 (2005).

[39] J. Nitta, T. Akazaki, H. Takayanagi, and T. Enoki, Phys. Rev. Lett. **78**, 1335 (1997).

[40] T. Oguchi and T. Shishidou, J. Phys. Condens. Matter **21**, 092001 (2009).

[41] E. Simon, A. Szilva, B. Ujfalussy, B. Lazarovits, G. Zarand, and L. Szunyogh, Phys. Rev. B **81**, 235438 (2010).

[42] L. Van Hove, Phys. Rev. **89**, 1189 (1953).

[43] I. M. Lifshitz, Sov. Phys. **11**, 1130 (1960).

[44] G. Dresselhaus, Phys. Rev. **100**, 580 (1955).

[45] S. Döhrmann, D. Hägele, J. Rudolph, M. Bichler, D. Schuh, and M. Oestreich, Phys. Rev. Lett. **93**, 147405 (2004).

[46] J. D. Koralek, C. P. Weber, J. Orenstein, B. A. Bernevig, S.-C. Zhang, S. Mack, and D. D. Awschalom, Nature (London) **458**, 610 (2009).

[47] I. Tokatly and E. Sherman, Ann. Phys. (NY) **325**, 1104 (2010).

[48] E. Frantzeskakis and M. Grioni, Phys. Rev. B **84**, 155453 (2011).

[49] H. Bentmann, F. Forster, G. Bihlmayer, E. V. Chulkov, L. Moreschini, M. Grioni, and F. Reinert, Europhys. Lett. **87**, 37003 (2009).

[50] L. Moreschini, A. Bendounan, H. Bentmann, M. Assig, K. Kern, F. Reinert, J. Henk, C. R. Ast, and M. Grioni, Phys. Rev. B **80**, 035438 (2009).

[51] F. Meier, H. Dil, J. Lobo-Checa, L. Patthey, and J. Osterwalder, Phys. Rev. B **77**, 165431 (2008).

[52] H. Zhang, C.-X. Liu, X.-L. Qi, X. Dai, Z. Fang, and S.-C. Zhang, Nat. Phys. **5**, 438 (2009).

[53] J. Henk, Phys. Rev. B **64**, 035412 (2001).

[54] W. H. Press, S. A. Teukolsky, W. T. Vetterling, and B. P. Flannery, *Numerical Recipes in Fortran 90: The Art of Parallel Scientific Computing*, 2nd ed. (Cambridge University Press, Cambridge, 1996), Vol. 2.